Virginia Tech 2023 Physics REU
July 24, 2023

Analyzing Neutral Hydrogen and Midplane Pressure in NGC 3941

Jessica Burns[1,2,4], Divij Garg[3,4], and Danielle Lucero[4]

[1] Department of Physics, University of Cincinnati, OH 45221, USA
[2] Department of Physics, Miami University, OH 45056, USA
[3] Department of Astronomy, University of Illinois Urbana-Champaign, IL 61801, USA
[4] Department of Physics, Virginia Polytechnic Institute and State University, VA 24061, USA

ABSTRACT

This paper presents a study conducted on NGC 3941, an early type galaxy, with the aim of examining its hydrogen content. The investigation of atomic (HI) and molecular (H_2) hydrogen composition in galaxies has proven valuable in understanding their structural characteristics, such as kinematics of gas, star formation tendencies, and crucially the hydro-static mid-plane pressure (HSMP) (Walter et al., 2008). Previous research has established relations between R_{mol}, the molecular to atomic hydrogen surface density ratio, and the hydro-static mid-plane pressure, P_{HM}. Specifically, the THINGS study examined 34 spiral galaxies and found that R_{mol} exhibits a proportionality to $P_{HM}^{0.8}$ (Walter et al., 2008). However, this relationship primarily derives from observations of spiral galaxies, implying that early-type galaxies might exhibit distinct characteristics that lead to a different correlation. Early-type galaxies diverge from spiral galaxies when considering their stars' radial orbits, absence of spiral arms, and lower levels of star formation activity. Furthermore, the ATLAS^{3D} study reported a disparity in the amount of atomic hydrogen (HI) present in early-type galaxies compared to spiral galaxies (Serra et al., 2012). Consequently, the focus of this paper centers on NGC 3941, an early-type galaxy known for its significant HI content, in order to test the previously established THINGS proportionality. In addition to providing high resolution HI data, we find that NGC 3941, despite being an early-type galaxy, more closely resembles the proportionality for spiral galaxies. This investigation is part of a broader study on the distribution of HI in 32 early-type galaxies. The study employs data obtained from the Very Large Array (VLA) B, C, and D arrays, enabling a comprehensive analysis of the hydrogen content within NGC 3941.

Introduction

Motivation

The study of neutral hydrogen in both spiral and early-type galaxies through radio astronomy has provided valuable insights about star formation and their properties within galaxies. Using the spin flip transition, atomic hydrogen can be observed at the 21 cm wavelength through the radio spectrum, often providing information about galaxies that is missing from optical observations. For example, using the known emission/absorption wavelength, atomic hydrogen can be used to detect doppler shifts within a galaxy, since we can compare the observed wavelength to the expected rest wavelength of 21 cm, allowing us to observe its kinematics (Liu et al., 2008). Moreover, hydrogen disks can extend far beyond the optical range of galaxies, indicating large gas rings and areas of future gas formation.

Primarily, such observations of hydrogen are done through interferometric arrays like the Very Large Array (VLA), utilizing multiple antennas to increase resolution and detection of faint objects. Single dish radio antennas do exist, but they have to be massive to have sufficient angular resolution. Interferomters, however, can increase angular resolution by placing antennas further away from each other. Hence, the VLA has 4 configurations, with A array having the antennas the furthest from each other, so a small angular resolution, while D array being the closest, so a high angular resolution. A combination of these arrays produce high resolution, detailed images of galaxies in the radio spectrum.

Using such interferometers, a key property of galaxies that has been studied is an empirical correlation between the surface density ratio $R_{mol} = \Sigma_{H_2}/\Sigma_{HI}$ and the hydrostatic midplane pressure (HSMP), P_{HM}, which is the hydrostatic pressure caused by stars and gas exerted upon the central plane of the galaxy. HI and H_2 are heavily associated with star formation, being cold neutral gasses. Hence, determining the amount of neutral hydrogen in galaxies has been important for detailed analyses, and the HSMP has been found to be to proportionate to R_{mol}. The THINGS study found that $R_{mol} \propto P_{HM}^{0.8}$ in a study of 34 spiral galaxies (Walter et al., 2008). This was a critical result, as it allows for the prediction of gas content based on the HSMP of a galaxy, which can aid in detection of H_2 given it does not have an emission line like HI. Yet, when stress-testing this relationship for early-type galaxies, slightly different correlations have been detected, with NGC 3941 serving as more data to better understand this trend (Lucero et al., 2023). A key reason for this lies in the dominating factors for HSMP in spiral vs early-type galaxies. While spiral galaxies are often dominated by star pressure, such assumptions do not necessarily hold for early-type galaxies. Hence, proportionalites based on spiral galaxies may not apply to early-type galaxies.

NGC 3941

Property	Value	Unit
Type	Early-Type	-
RA	178.2306	Deg
Dec	36.9863	Deg
Diameter	12.37	kpc
z (Helio)	0.00308	-
Inclination	57.9	Deg
Hubble Distance	17.47	Mpc

Table 1: Information about NGC 3941. Sourced from NASA Extragalactic Database.

NGC 3941 is part of a larger diverse sample of 32 early-type galaxies that have been selected based on their HI and CO content. Alongside being HI-rich and CO-poor, this galaxy has been studied extensively in the past due to its unique properties (Young et al, 2011). Fisher et al., 1997 reported that it contains a counter-rotating gas disk that extends past the optical range of the galaxy, potentially caused by a past merger event, which are often seen in the history of early-type galaxies. Erwin & Sparke, 2002 reported that it's a double-barred galaxy, meaning there's a central bar within the galaxy that contains another smaller bar. Laurikainen et al., 2005 found 4 arc second inner spirals within the galaxy. These features are relatively visible in our images of NGC 3941 and optical images, and they will be important to understanding our results of the galaxy.

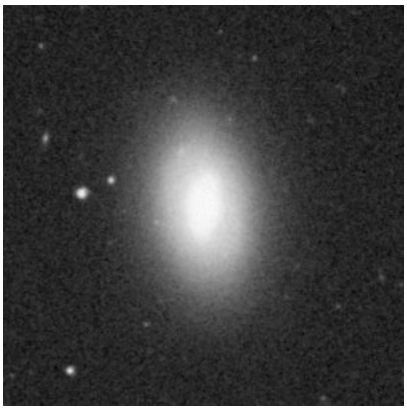

Figure 1: DSS2 Red Image of NGC 3941 (McGlynn et al., 2008)

Structure of Paper

The paper begins by providing information about our data collection process and then goes into our methodology behind computing the HSMP. We then provide HI images of NGC 3941 and a discussion of the observed results, followed by broader conclusions and unanswered questions.

Theoretical Framework

Our analysis of NGC 3941 relies on the HI, H_2, and HSMP of the galaxy. HI data was obtained by data reduction of VLA images,and ultimately used to compute azimuthal averages for the HI surface density. $H_2$and HSMP required other frameworks.

H_2 Data

NGC 3941 is undetected in CO. We utilize an upper limit of the H_2 mass from Young et al. 2011 (from single dish) to derive an upper limit to the H_2 surface density. Young et al. 2011 use the typical CO to H_2 conversion factor derived for the Milky Way to arrive at their H_2 mass upper limit. We assume that any CO in this galaxy will be distributed in a disk with a radius equal to the effective radius (R_e = 2.0 kpc). We then derive an upper limit to the H_2 surface density by simply dividing the H_2 mass by the area of the disk. This gives an upper limit to the H_2 surface density of $\Sigma_{H2})< 0.62$ $M_\odot$ pc^{-2}. We also assume that the CO will be distributed in an exponential disk with peak CO surface density equal to the derived upper limit.

$$\Sigma_{H_2}(R) = 0.62 * e^{(-R/2.0\ \mathrm{kpc})} ...(M_\odot pc^{-2})$$

Hydrostatic Midplane Pressure

The equation we use for hydrostatic midplane pressure was determined by Lucero et al., 2023, and is referenced below.

$$P(0) = G\Sigma_g^2 + [(G\Sigma_g^2)^2 + 2G\Sigma_g^2\rho_s\sigma_g^2]^{1/2}.$$

Here, σ_g is the gas velocity dispersion (8 km/s), ρ_s is the stellar volume density, Σ_g is cold gas surface density. ρ_s was determined from Multi Gaussian Expansion fits to a K-band Spitzer image (Cappellari, 2002). K-band traces the older stellar populations which dominated in early-type galaxies. As we'll describe later, we computed these values at different radii to create our graph of R_{mol} vs P_{HM}.

Data Analysis

VLA Data

Our data was taken with JVLA B, C, and D array configurations between 2014-2019. We used 3C286 as our bandpass/flux calibrator and J1227+3635 as our phase calibrator. The phase calibrator was observed every twenty minutes. Detailed information is given in Table 2.

Reduction and Calibration

We conducted the data reduction process using an older version (5.6.2) of CASA (Common Astronomy Software Applications), a software package for radio astronomy data analysis. The data reduction steps involved in this study aimed to process the raw observational data obtained from the NGC 3941 galaxy. Initially, we employed the CASA task listobs to gather essential information about each measurement set. The listobs command provided us with detailed insights into observation specifics, including observation details, data records, and spectral windows. This information proved crucial for data analysis and interpretation.

To gain further understanding of the data, we first examined the positions the antenna were in during our observation. By visualizing the antenna positions, we could assess their distribution and identify and reference antenna that was in close proximity to the center. Selecting a reference antenna in such a manner helped ensure more accurate calibration.

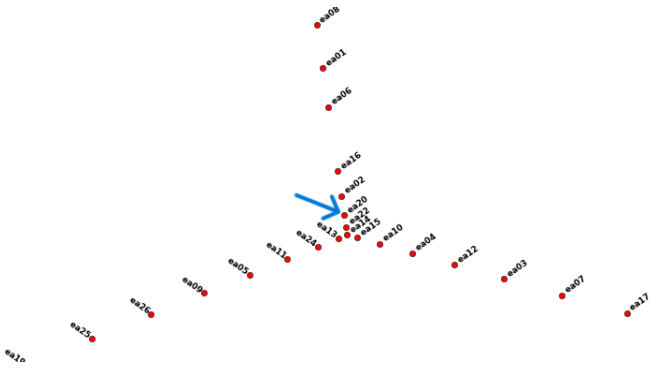

Figure 2: Configuration of VLA antennas during the initial data collection for the C array on day 1. The antenna indicated by the blue arrow corresponds to ea 20, which serves as the selected reference antenna for this dataset.

To facilitate data inspection, we created channel zero data sets for each target of interest using the oldsplit task within CASA. This involved averaging the middle 75% of channels

within each data set into a single channel. By condensing the spectral information into a single channel, we simplified the data inspection process while preserving the overall signal characteristics.

We then flagged problematic data in order to exclude it from subsequent analysis. We utilized the CASA viewer and the plotms task to inspect the data visually and identify any anomalies or artifacts. We carefully examined the data related to the flux/bandpass calibrator, phase calibrator, and target, aiming to flag any data points affected by external factors such as storms or instrumental issues. These and multiple other sources could lead to bad data, including shadowing caused by low elevation during the observation. To ensure the accuracy and reliability of our analysis, we flagged any shadowed data points that might introduce inaccuracies into the results. By carefully flagging and excluding the affected data, we minimized the impact of these external factors.

The calibration process is a critical stage in ensuring the accuracy of the data sets. We followed a calibration procedure which included the following steps:

1. Antenna position calibration: We performed an antenna position calibration to accurately determine the positions of the antennas within the array. This calibration step corrected for any residual errors or uncertainties in the measured antenna positions, ensuring precise spatial localization of the sources

2. Gain curve calibration: We applied gain curve calibration to correct for any variations in the sensitivity of the individual antennas as a function of frequency. This calibration step accounted for the frequency-dependent response of the antennas, allowing for accurate flux density measurements

3. Delay calibration: Delay calibration was performed to compensate for the differences in signal arrival times at the various antennas due to their varying distances from the source. By accurately estimating and correcting for these delays, we achieved improved phase coherence and precise determination of the source positions.

4. Initial bandpass calibration: The initial bandpass calibration is a phase-only gain calibration, where we derived the complex antenna gains without considering the frequency-dependent bandpass shape.

5. Actual bandpass calibration: The actual bandpass calibration was performed to determine the frequency response of the system, accounting for any variations in the bandpass shape across the observation band. By incorporating the frequency-dependent variations in the system response, this step refined the bandpass solutions.

6. Main gain calibration: The main gain calibration involved phase calibration for intervals solint='int' and scans solint='inf'. We derived the gain solutions to correct for both amplitude and phase variations across time, ensuring accurate flux density measurements and phase coherence.

7. Additional gain calibration: If necessary, we performed additional gain calibration steps using different parameters to further refine the calibration. This included utilizing infinite solution intervals (solint='inf') and performing simultaneous amplitude and phase calibration (calmode='ap'). These additional steps ensured the accuracy and robustness of the final calibration solutions.

Imaging and Spectral Analysis

Having completed the calibration process, we proceeded to generate images to visualize the data and assess the quality of the calibration. To create continuum images for each relevant field, we begin by splitting the calibrated data into separate measurement sets, using the oldsplit task in CASA to create channel zero data sets. The splitting process involved averaging all channels into a single channel, facilitating easier inspection and analysis. After splitting the data, we performed the following steps to generate images for each field and assess the quality of the calibration.

Using the CASA clean task, we initially generated dirty images for each field. The niter parameter was set to zero to create a dirty image that revealed the presence of the source and any potential artifacts. To improve the image quality and identify any remaining artifacts, we performed a second round of imaging using the clean task. The cleaning algorithm was applied itera-

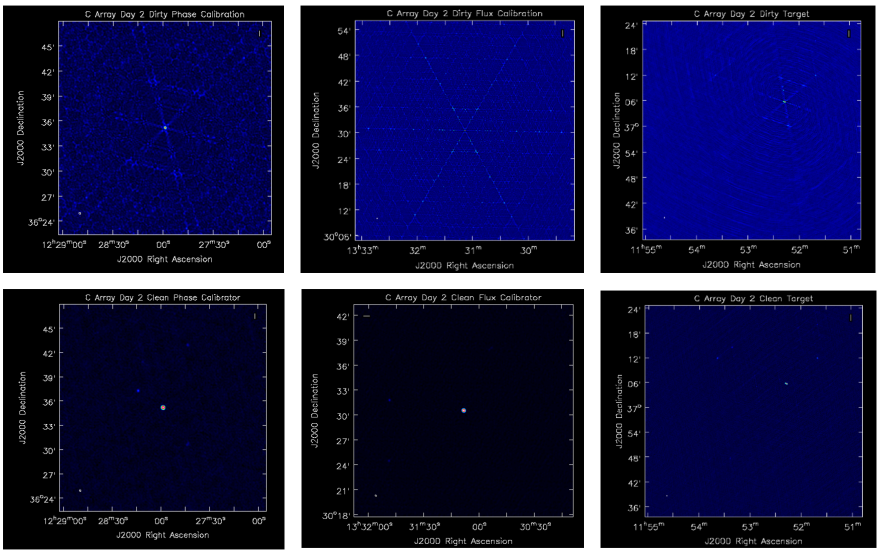

Figure 3: Before and after cleaning the different fields for our data from day 2 of the C array. The left images are the phase calibrators, the middle images are the flux calibrators, and the right images are the targets.

tively by specifying a higher value for the niter parameter. The resulting cleaned images allowed for a detailed examination of the sources (see Figure 3).

To evaluate the noise level in the cleaned images, we measured the root mean square (RMS) noise. This involved selecting a region in the image that contained no significant signal, preferably near the phase center. By placing a box around this region, we observed the RMS noise value. Multiple measurements were taken at different locations within the image to ensure reliability. The measured RMS noise was then compared to the theoretical value obtained using the formula:

$$\text{RMS Noise} = \frac{8}{\sqrt{N * (N-1) * dV * T_s * \#IFs}},$$

where N is the number of telescopes in the array during the observations, dV is the width of a channel in MHz (75% of the total bandwidth in this case), T_s is the total time on target in hours, and #IFs is the total number of spectral windows. This equation provides the theoretical RMS noise value in millijanskies per beam.

The generated images and the measured RMS noise provided valuable insights into the quality of the calibration and the data itself. They allowed us to visually inspect the sources, identify potential artifacts or sidelobes, and assess the overall image quality. The comparison between the measured RMS noise and the theoretical value helped validate the accuracy of the observations and the subsequent analysis.

With the calibrated and cleaned continuum images in hand, we proceeded to perform continuum subtraction to isolate the HI line emission. To remove the continuum contribution from the data and focus on the HI line emission, we utilized the uvcontsub task in CASA. Based on previous observations, we determined that the HI line has a width of approximately 200 km/s, while the native resolution of the data is 3.3 km/s. Hence, we excluded approximately 61 channels (200/3.3) centered around the central channel from the continuum fitting process. The uvcontsub task was executed with the specified parameters, including the measurement set (vis) and the spectral window (fitspw) for continuum fitting.

After performing the continuum subtraction, we set the rest frequency and systemic velocity of the source to correct for the Doppler effect during the subsequent imaging process. The rest frequency was set to 1.420406 GHz, and the systemic velocity of NGC 3941 (922 km/s) was converted to meters per second (m/s) and set accordingly using the CASA Table Toolbox (tb) commands. This step ensured accurate velocity calibration during the imaging process.

Following the continuum subtraction and velocity calibration, we generated dirty image cubes of the continuum-subtracted data using the clean task. Two sets of image cubes were created, one with a robust parameter of zero (maximizing resolution) and the other with a natural weighting scheme (maximizing sensitivity at the expense of resolution). The cubes were generated with a width of 16 channels (24 km/s wide channels) to allow for some averaging. The generated image cubes were visually inspected using the CASA viewer to identify the presence of HI emission in the central channels. Additionally, we measured the RMS noise in several channels of each cube to assess the noise level. This involved selecting regions within the cubes that contained no significant signal, preferably near the phase center, and calculating the RMS noise values. Multiple measurements were taken in different channels to ensure accuracy. The measured RMS noise values were then compared to the theoretical value obtained using Eq. (1).

Upon confirming that the measured RMS noise is within 10 percent of the expected values, we can proceed to the next data set. Once all epochs of our C, B, and D array data are calibrated and continuum-subtracted, they will be imaged together in various ways to create comprehensive data sets.

Data Combination and Moment Maps

The subsequent step in our analysis involves the combination of the prepared data epochs through the application of different weightings. Specifically, we investigate combinations of the B, C, and D arrays with natural and robust weightings.

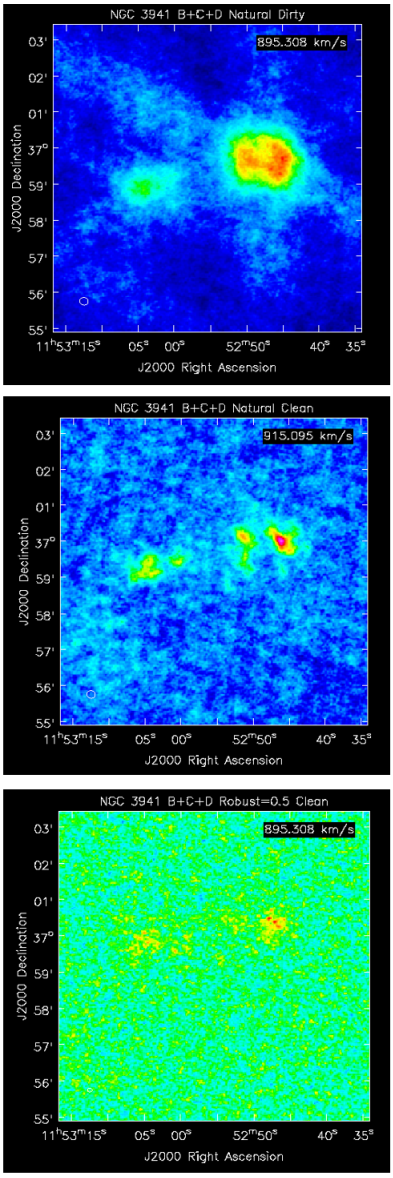

Figure 4: Before and after cleaning one channel of B+C+D. On top is the dirty image, the middle is the cleaned naturally weighted image, and on the bottom is the cleaned robustly weighted image

To ensure consistency, we verify that all epochs share the same systemic velocity (922 km/s) using CASA's listobs task.

Channel widths are standardized across the arrays by employing the split task. The weights for each epoch are determined via the statwt command, which quantifies visibility scatter or RMS noise. Notably, the C array exhibits heightened sensitivity, warranting higher weighting compared to the B and C arrays.

With the data primed for analysis, we proceed to generate combined images. Following a process similar to cleaning individual day data, we initially construct a naturally weighted dirty cube using the clean task, noting its corresponding RMS noise away from the HI continuum. Likewise, a dirty cube with robust=0 weighting is created, with the RMS noise from both cubes serving as the cleaning threshold to prevent excessive iterations. Subsequently, the cube undergoes an extensive cleaning process by setting a large niter value in the clean task, wherein the HI continuum is identified and removed. This iterative procedure is repeated for each array and epoch combination, facilitating comprehensive analysis of the combined data (see Figure 4 as an example).

Now the data can be imaged together. It is a similar process to cleaning one day of data; first, a naturally weighted dirty cube is created using the clean task, and its RMS noise will be noted. The same is done for a dirty cube with robust=0 weighting. This RMS noise will be the threshold for cleaning, so the cleaning process doesn't go too far. Then, the cube is cleaned by raising the niter specification to a large number, and the HI continuum is marked and cleaned. This process is repeated for each combination of arrays and epochs.

Then, the generation of moments maps is undertaken to capture relevant information about each combination. This involves leveraging the cleaned cube and utilizing the mask derived from the cleaned cube. By employing the immoments task, we can specify the spectral channels that exhibit hydrogen emission, enabling the extraction of the desired moments.

Azimuthal Averaging

Proceeding to the azimuthal averaging stage, we begin by exporting our moment 0 maps to FITS format using the CASA task exportfits. Following this, we exit CASA and initiate the Miriad software environment. To load the data into Miriad, we use the fits task with the xyin option to convert the FITS formatted moment maps to the Miriad format.

For visualization purposes, we can utilize the "cgdisp" task in Miriad to view the moment maps. By specifying the input Miriad file and the display options, we can examine the maps interactively.

To perform azimuthal averaging, we employ the Miriad task "ellint," which fits elliptical annuli to the HI distribution. The task requires input parameters such as the input Miriad file, output residual image filename, center coordinates of the HI distribution, position angle (PA) of the galaxy, inclination along the line of sight, and radius specifications for the annuli. The resulting azimuthal averages are saved in a text file.

Finally, we can plot the H_2/HI surface density versus Hydrostatic Midplane pressure using a Python script.

Results

We first present overall results displaying plots from all of our configurations, and then focus specific trends on the B+C+D Natural and Robustly weighted graphs within our conclusions. Those were the configurations we utilized for our study. Detailed configuration data for our study is given in Table 2.

First, we display moment maps of NGC 3941 taken with various array configurations allowing for different beam sizes in Figure 7. The variation in beam sizes allows for different HI regions to be resolved and displays general trends within the galaxy. Figure 7, with the exception of 7h, are high resolution HI images of NGC 3941. Past ATLAS^{3D} images of NGC 3941 had a 39" beam size, whereas our images provide 14" and 9" images, further resolving the HI (Serra et al., 2012). Figure 7h represents the largest beam size at ~ 65", taken with the D array, while Figure 7d represents the smallest beam size at ~6".

Next, we present contour maps made using the Sloan Digital Survey image and 4 configurations of the VLA in Figure 8 (McGlynn et al., 2008) These contour maps were made by overlaying VLA maps over an SDSS image of NGC 3941, allowing us to observe the HI distribution in the context of the optical range of the galaxy . We only present the B+C+D and C+D images for the contour maps.

Moving on, using the moment maps in Figure 7, we create azimuthal averaging for the HI surface density with all of the configurations, allowing us to view the surface density of HI at different radii within the galaxy (see Figure 5).

Finally, we present results on the R_{mol} to pressure ratio (Figure 6). The values were calculated with $0, 7, 14, 21, 28$, and 35 arcsec with the naturally weighted B+C+D moment map (Figure 7a). We used the HSMP equation mentioned earlier to calculate the values at the different radii.

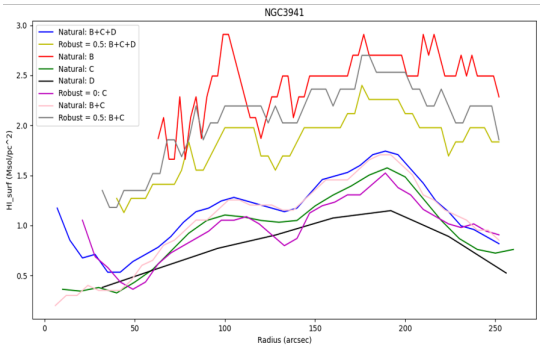

Figure 5: The radial HI surface density distribution derived from azimuthal averages in the HI maps. Higher resolution images detect higher density HI, but resolve out the more diffuse HI In the center.

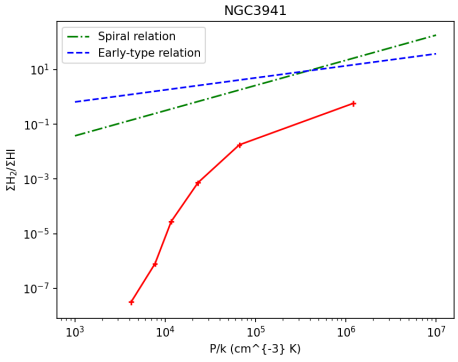

Figure 6: Ratio of H_{mol} to pressure. The red line depicts the results from NGC 3941. The spiral relation is from THINGS Walter et al., 2008, while the early-type relation is from Lucero et al. 2023.

Config	Weighting	Flux Cal	Phase Cal	Δv (km/s)	Beam (arcsec)	Beam (kpc)	Chan	RMS Noise (Jy/beam)
B+C+D	Natural	3C286	J1227+3635	20	14.1"x12.6"	1.19x1.06	170	$1.8 * 10^{-4}$
B+C+D	Robust = 0.5	3C286	J1227+3635	20	7.8"x5.7"	0.66x0.48	170	$2.1 * 10^{-4}$
B+C	Natural	3C286	J1227+3635	20	12.5"x10.1"	1.05x0.85	170	$1.9 * 10^{-4}$
B+C	Robust = 0.5	3C286	J1227+3635	20	7.0"x5.4"	0.59x0.46	170	$2.2 * 10^{-4}$
C	Natural	3C286	J1227+3635	20	10.5"x17.2"	0.89x1.45	64	$1.9 * 10^{-4}$
C	Robust = 0	3C286	J1227+3635	20	14.1"x12.0"	1.19x1.01	64	$2.3 * 10^{-4}$
B	Natural	3C286	J1227+3635	20	6.2"x 4.9"	0.52x0.41	170	$2.1 * 10^{-4}$
D	Natural	3C286	J1227+3635	20	65.6"x 52.3"	5.53x4.41	85	$5.0 * 10^{-4}$

Table 2: NGC 3941 Data Observation. Here, Δv refers to the channel width, the beam in arcseconds refers to the angular beam size and the beam in kiloparsecs refers to the linear beam size. Finally, RMS noise is derived from the line free channels.

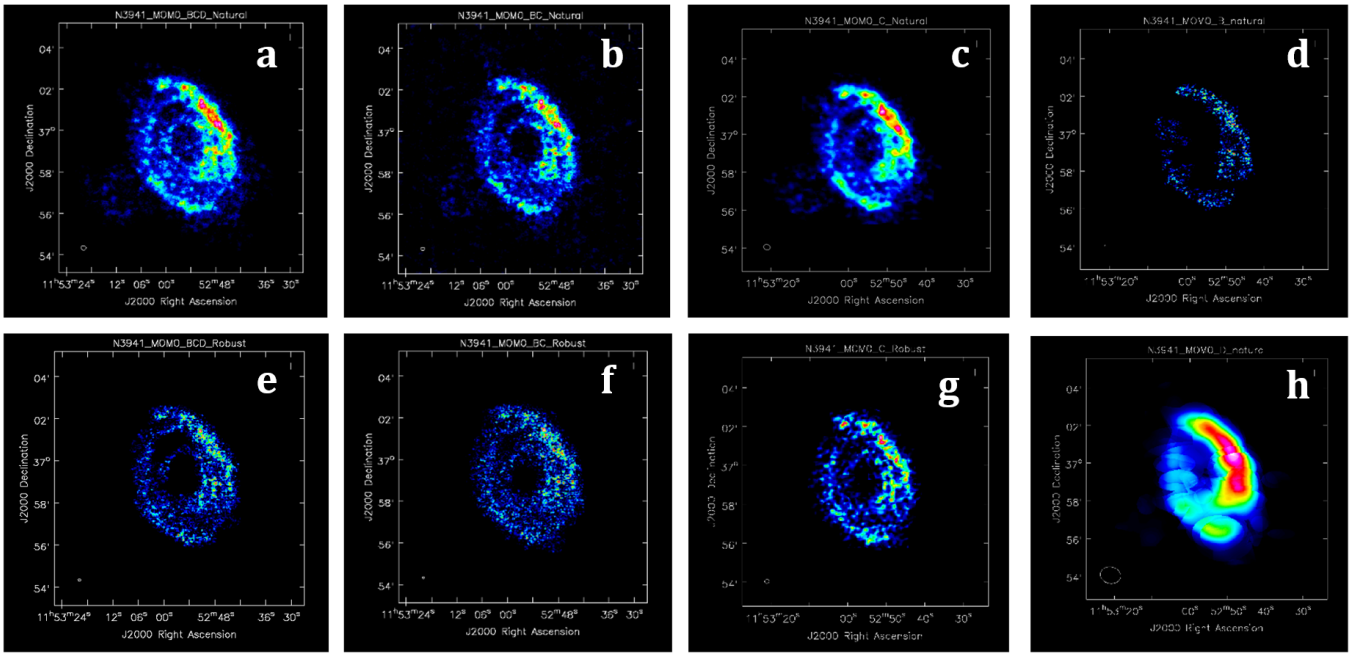

Figure 7: In the top row, from left to right, we have the moment maps of: B+C+D array natural weighting, C+B array natural weighting, C array natural weighting, and B array natural weighting. In the bottom row, from left to right, we have the moment maps of: B+C+D array robust=0.5 weighting, C+B array robust=0.5 weighting, C array robust=0 weighting, and D array natural weighting.

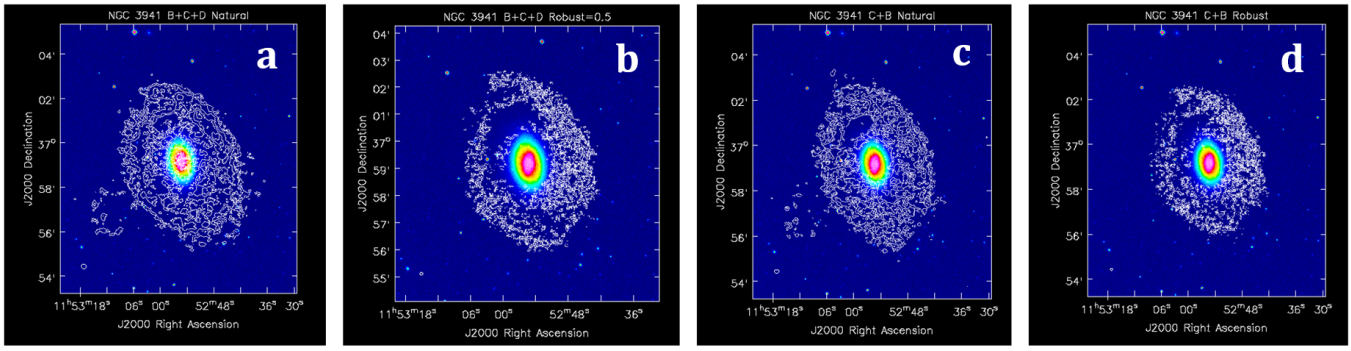

Figure 8: SDSS 2 Image of NGC 3941 overlayed with various contour maps; from left to right: B+C+D natural weighting (peak HI intensity=0.12 Jy/beam*km/s), B+C+D robust=0.5 weighting (peak HI intensity=0.062 Jy/beam*km/s), C+B natural weighting (peak HI intensity=0.098 Jy/beam*km/s), C+B robust=0.5 weighting (peak HI intensity=0.051 Jy/beam*km/s). The relative contour levels used are 10%, 20%, 40%, 60%, and 80% of the HI peak.

Conclusions and Discussion

HI Distribution

Within our HI azimuthal averaging in Figure 5, four key features emerge. NGC 3941 starts with a sharp dip in HI surface density to around 45 arcsec, and then peaks around 100 arcsec and ~175 arcsec. The initial peak in HI represents a dense cluster of HI at the center of the galaxy. The HI dip represents an HI hole while the peaks represent two distinct rings of HI, which were previously detected (Van Woerden et al., 1983).

Van Woerden et al., 1989 gives a likely reason for these observations, claiming that the bar in the center of NGC 3941 has the potential to clear HI gas through energy shocks in the inner region. The non-axisymmetrical bar could then drive HI outwards towards the inner HI ring while also channel HI towards the center of the galaxy, leading to dense HI in the center and the inner HI ring in NGC 3941 (Murugeshan et al., 2023). The region between the center and first HI ring would then be clear of HI visible in the moment maps and azimuthal average as an HI hole. Alongside that, the presence of an outer bar (since this is a double-barred galaxy) could be the cause of the second HI ring. Through a similar effect, the outer bar could drive HI towards the outer HI ring of the galaxy and channel HI towards the inner HI ring. However, further analysis is needed to truly test this theory. Another reason is given by Fisher et al. 1997, claiming that this HI gas was likely acquired through a merger or accretion event and has now settled in equilibrium. Given that this is a counter-rotating gas disk, this could be a viable explanation.

R_{mol} to Pressure Relationship

Figure 6 represents the main focus of our work, the relationship between R_{mol} and HSMP. We display an unexpected trend within the galaxy. The slope of the R_{mol} to pressure line much closely resembles the spiral slope within the central area derived from previous results, rather than the early-type slope currently being worked on by Lucero et al., 2023. An explanation of the deviation could lie within the location of HI and the spiral features discussed earlier. NGC 3941 contains two spiral arms, and while the significance of these spiral features is small, if spiral features have sufficient high stellar volume density, then star pressure would dominate the HSMP equation, making it much more closely resemble a spiral galaxy. Alongside that, a significant majority of the HI within this galaxy lies outside the optical range of the galaxy, meaning it is possible that this HI has not reached the inner parts of the galaxy resulting in lower HI surface density in the optical radius. Hence, the pressure in the optical disk could likely be dominated by stars, not gas, similar to spiral galaxies. These could be potential explanations for why NGC 3941 is unique amongst early-type galaxies.

Further Discussion

In Figure 8, it becomes clear that the majority of HI is not in the optical range of the galaxy and rather lies in a gas disk beyond that range. In the inner parts of the galaxy, the HI isn't as abundant due to the bar structure. In the outer parts of the galaxy, the HI is widely diffuse due to a larger radius. Hence, both result in low HI surface density when compared to other galaxies. Reasons for this should be investigated as it may impact the relationship between R_{mol} and HSMP.

The lack of CO within the galaxy makes calculating Σ_{H_2} beyond 35 arcsec difficult given an exponential decrease with increasing radius. Hence, our calculation for the HSMP stops at 35 arcsec due to unreliability of H_2 data beyond this limit. In addition, the CO/H_2 conversion factor used by Young et al., 2011 relies on data from the Milky Way Galaxy, a spiral galaxy. Future analysis on this ratio for early-type galaxies could yield different results, especially given the different properties of early-type galaxies.

This galaxy was part of a larger study of 32 early-type galaxies being analyzed in high resolution HI images to stress-test the spiral relationship shown in Figure 6. Future studies will expand on those galaxies and highlight more differences between spiral and early-type galaxies.

Acknowledgements

We thank Dr. Lucero for her mentorship and guidance this summer as well as Krislyn Sourivong, Debra Dunham, and Ishan Sobti for their contribution to the project. We further acknowledge the outstanding support from the National Science Foundation and the Virginia Tech Physics department. This work was made possible by the National Science Foundation under grant No. PHY-2149165. This research has made use of the NASA/IPAC Extragalactic Database (NED), which is operated by the Jet Propulsion Laboratory, California Institute of Technology, under contract with the National Aeronautics and Space Administration. This work is based [in part] on observations made with the Spitzer Space Telescope, which was operated by the Jet Propulsion Laboratory, California Institute of Technology under a contract with NASA.

References

Cappellari, Michele. "Efficient Multi-Gaussian Expansion of Galaxies." Monthly Notices of the Royal Astronomical Society, vol. 333, no. 2, 2002, pp. 400–410.

Erwin, Peter, and Linda S. Sparke. "Double Bars, Inner Disks, and Nuclear Rings in Early-Type Disk Galaxies." *arXiv.Org*, 29 Mar. 2002.

Fisher, David. "Kinematic Profiles of S0 Galaxies." *The Astronomical Journal*, vol. 113, 1997, p. 950.

Laurikainen, Eija, et al. "Multicomponent Decompositions for a Sample of S0 Galaxies." *Monthly Notices of the Royal Astronomical Society*, vol. 362, no. 4, 2005, pp. 1319–1347.

Liu, Lola, and Chris Chronopoulos. "The Hydrogen 21-Cm Line and Its Applications to Radio Astrophysics." MIT, 9 Mar. 2008.

Lucero, D., et al. (2023). *The H2-HI Transition in Early-Type Galaxies: The Rmol-Pressure Relation II*. [Manuscript in preparation]. Department of Physics, Virginia Tech.

McGlynn, T., Scollick, K., White, N., SkyView: The Multi-Wavelength Sky on the Internet, McLean, B.J. et al., New Horizons from Multi-Wavelength Sky Surveys, Kluwer Academic Publishers, 1996, IAU Symposium No. 179, p465.

McMullin, J. P., Waters, B., Schiebel, D., Young, W., and Golap, K. 2007, Astronomical Data Analysis Software and Systems XVI (ASP Conf. Ser. 376), ed. R. A. Shaw, F. Hill, and D. J. Bell (San Francisco, CA: ASP), 127

Murugeshan, C., et al. "The HI in Ring Galaxies Survey (HI-Rings)—Effects of the Bar on the HI Gas in Ring Galaxies." *Publications of the Astronomical Society of Australia*, vol. 40, 2023.

Sault R.J., Teuben P.J., and Wright M.C.H., 1995. "A retrospective view of *Miriad*." *Astronomical Data Analysis Software and Systems IV*, ed. R. Shaw, H.E. Payne, J.J.E. Hayes, ASP Conference Series, 77, 433-436.

Serra, Paolo, et al. "The ATLAS3D Project - XIII. Mass and Morphology of HI in Early-Type Galaxies as a Function of Environment." Monthly Notices of the Royal Astronomical Society, vol. 422, no. 3, 2012, pp. 1835–1862.

Van Rossum, G., and Drake, F. L. (2009). Python 3 Reference Manual. Scotts Valley, CA: CreateSpace.

Van Woerden, Hugo, et al. "Distribution and Motions of Atomic Hydrogen in Lenticular Galaxies." *Internal Kinematics and Dynamics of Galaxies*, 1983, pp. 99–104.

Walter, Fabian, et al. "Things: The Hi Nearby Galaxy Survey." *Astrophysics and Space Science Proceedings*, 2008, pp. 97–104, https://doi.org/10.1007/978-1-4020-6933-8_21.

Young, Lisa M., et al. "The ATLAS3D Project - IV. the Molecular Gas Content of Early-Type Galaxies." *Monthly Notices of the Royal Astronomical Society*, vol. 414, no. 2, 2011, pp. 940–967.